International Journal of Research in Engineering and Science (IJRES)
ISSN (Online): 2320-9364, ISSN (Print): 2320-9356
www.ijres.org Volume 14 Issue 2 ǁ February 2026 ǁ PP. 195-205

Improved Reconfigurable Terahertz Microstrip Antenna for Present and Future Wireless Communication Systems

Ogueri Chimezie Davies[1], Eseosa Omorogiuwa[2], Matthew Ehikhamenle[3]
*[123]*Centre for Information and Telecommunication Engineering (CITE), Faculty of Engineering,*
University of Port Harcourt, Port Harcourt, Nigeria
Corresponding Author: Ogueri Chimezie Davies

Abstract
This paper presents the design and modelling of a frequency-reconfigurable multiband terahertz (THz) microstrip patch antenna targeted at present and future wireless communication front ends. The antenna is realized on a quartz substrate (εr = 3.82) with a thickness of 80 μm, using a slot-loaded rectangular patch topology with switchable conductive bridge elements based on VO_2 and graphene to enable state-controlled resonance tuning. Using Maxwell scale invariance and a MATLAB-based simulation workflow, three switching states are obtained with resonances at approximately 0.30 THz (State A), 0.60 THz (State B), and 0.90 THz (State C). The simulated impedance response satisfies the −10 dB matching criterion in all states, with minimum S_{11} values of about −17 dB, −25 dB, and −15 to −16 dB, respectively. The corresponding −10 dB impedance bandwidths are 5.5 GHz (1.83%) at 0.30 THz, 9.6 GHz (1.60%) at 0.60 THz, and 10.0 GHz (1.11%) at 0.90 THz, with VSWR < 2 around each resonance. Radiation remains broadside and stable across states, with peak realized gain between 4.8–5.5 dBi and radiation efficiency peaking at approximately 39–53% depending on the operating band. Overall, the results verify that the proposed VO_2/graphene-enabled structure delivers clear, switch-driven multiband operation in the THz regime, supporting candidate applications in 6G/THz links and high-data-rate short-range THz systems.

Keywords: Terahertz antenna, microstrip patch, frequency reconfigurability, VO_2 switch, graphene, 6G.

Date of Submission: 07-02-2026 Date of Acceptance: 17-02-2026

I. INTRODUCTION

Sixth generation (6G) and beyond wireless systems are increasingly exploring the sub-terahertz and terahertz spectrum to unlock ultra-wide bandwidths, ultra-high data rates, and new sensing-communication integration paradigms. At these frequencies, antennas become physically compact, but design is constrained by severe free-space path loss, material dispersion, fabrication tolerances, and reduced radiation efficiency due to conductor and dielectric losses.

Microstrip patch antennas remain attractive due to their low-profile form factor, planar integration, and predictable resonance behaviour. However, conventional patches are inherently narrowband, and single-band operation is insufficient for multi-service 6G terminals. Reconfigurable antennas address this limitation by enabling on-demand tuning (frequency/polarization/pattern) using electrical, optical, or material switching mechanisms.

This work proposes a multiband THz microstrip patch antenna that achieves state-controlled frequency reconfiguration using switchable conductive bridges realized with VO_2 and graphene. The design targets three discrete operating bands centred near 0.30, 0.60, and 0.90 THz to represent down-shift, baseline, and up-shift modes, while maintaining consistent impedance matching and stable broadside radiation.

II. ANTENNA STRUCTURE AND METHOD

The antenna is implemented on a quartz (fused silica) substrate selected for low loss and dielectric stability at THz frequencies (εr = 3.82, thickness h = 80 μm). A rectangular microstrip patch with U-slot loading is used to elongate the current path and introduce additional resonant behaviour. A microstrip feed excites the patch, while a full ground plane provides the return path. Frequency reconfigurability is achieved by selectively shorting or opening slot regions with switchable conductive bridges (VO_2/graphene) that alter the effective electrical length of the radiator.

2.1 DESIGN WORKFLOW

Figure 1 summarizes the modelling workflow used to obtain the antenna responses across the three switching states.

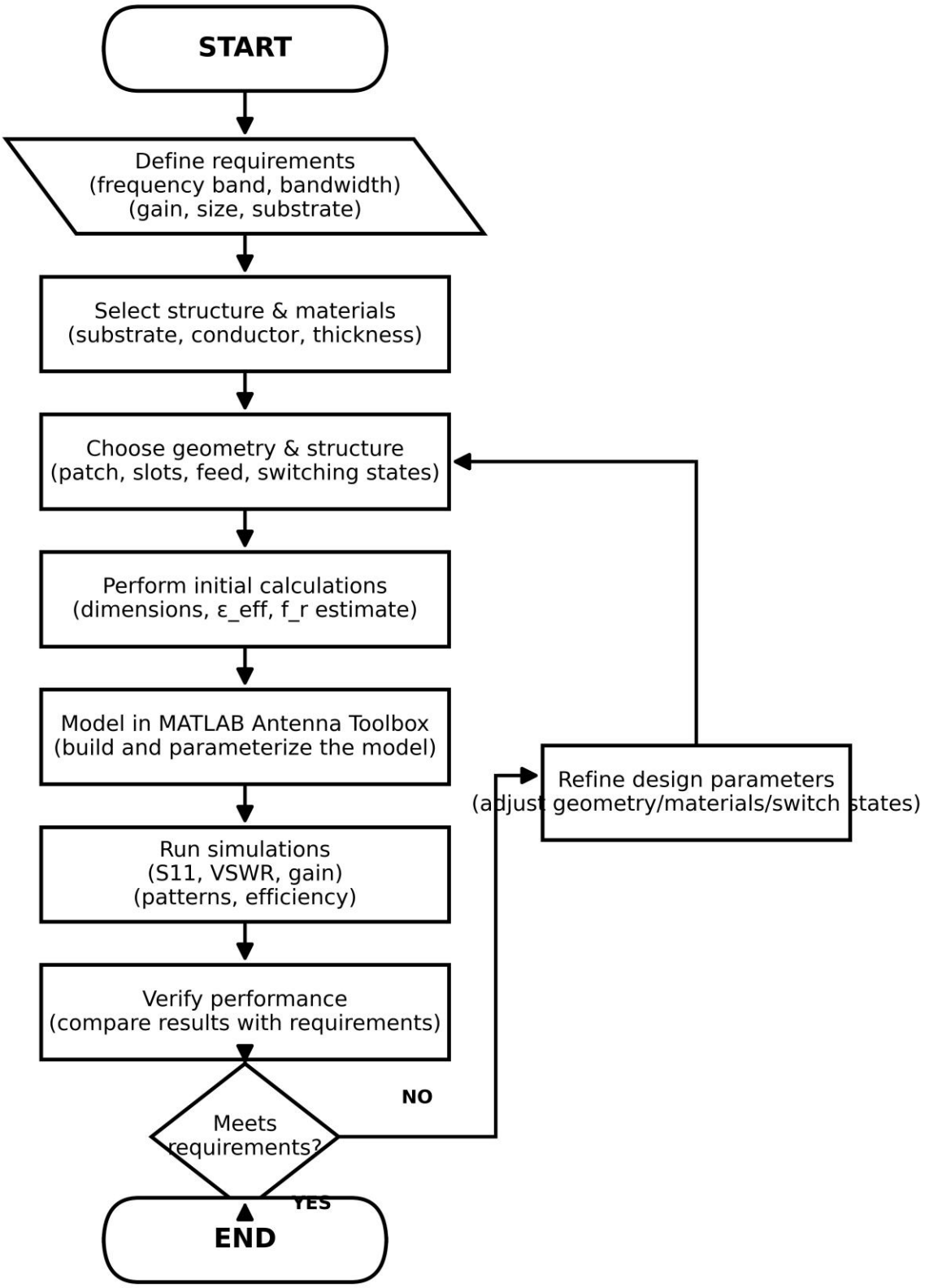

Figure 1: Research methodology and simulation workflow.

2.2 ANTENNA ARCHITECTURE AND GEOMETRY

The overall reconfigurable antenna system architecture and the adopted slot-loaded patch geometry are illustrated in Figures 2–4.

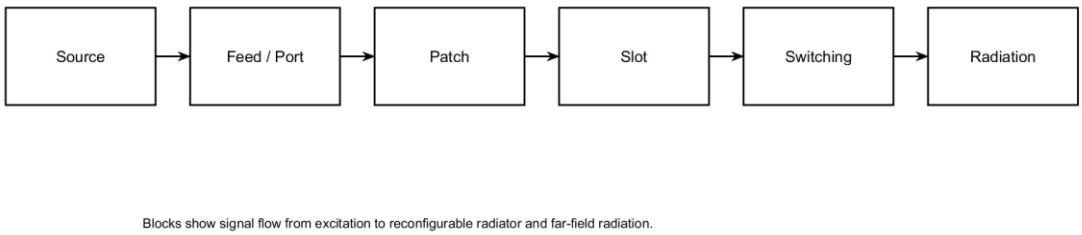

Figure 2: Overall reconfigurable antenna system architecture.

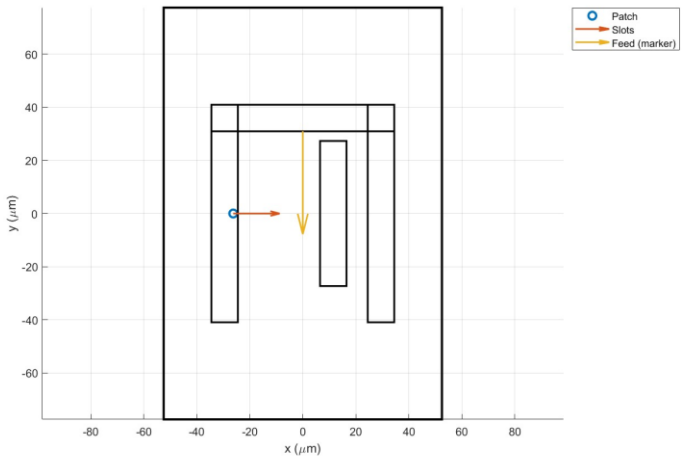

Figure 3: Slot-loaded rectangular microstrip patch geometry (top view).

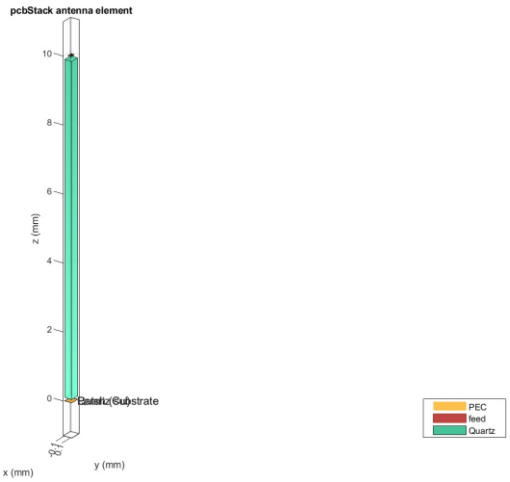

Figure 4: MATLAB antenna model (3D PCB stack representation).

2.3 RECONFIGURATION MECHANISM AND SWITCHING STATES

Reconfiguration is implemented through switchable conductive bridges placed across key slot and extension regions. When a bridge is ON (high conductivity), it effectively shorts a slot section, increasing the effective current path and shifting resonance downward. When OFF (low conductivity), the slot effect is restored, shortening the current path and enabling higher resonant states. Table 1 defines the state logic used in this work.

Table 1: Switch-state definition used to realize the three operating bands.

Reconfiguration element	Function	State A (Down-shift)	State B (Baseline)	State C (Up-shift)
U-slot bridge (top)	Shorts the U-slot Opening to reduce Slot effect/lengthen Effective current Path	ON	OFF	OFF
U-slot bridge (right/mid)	Additional short Across U-slot leg region (supports lower resonance)	ON	OFF	OFF
Patch extension Islands (top & bottom)	Extends effective radiator length (Shifts resonance downwards)	ON	OFF	OFF
Auxiliary slot Bridge	Alters coupling near the edge to shorten effective patch/shift resonance upward	OFF	OFF	ON

2.4 PERFORMANCE METRICS AND KEY CALCULATIONS

Impedance matching is evaluated using the reflection coefficient S_{11}. The voltage reflection coefficient magnitude is obtained from:

$$\Gamma = 10^{S_{11}/20}$$

$$\eta\_match = 1 - |\Gamma|^2$$

The −10 dB impedance bandwidth is defined as:

$$BW = F_{high} - F_{low}$$

Fractional bandwidth is computed as:

$$FBW = (BW / f_c) \times 100\%$$

Realized gain is obtained directly from the far-field solution and accounts for both radiation and matching losses.

III. RESULTS AND DISCUSSION

3.1 IMPEDANCE MATCHING AND BANDWIDTH

The simulated S_{11} responses for the three switching states are shown in Figure 5, while Figure 6 highlights the −10 dB bandwidth limits around each resonance. All states satisfy the −10 dB criterion with distinct resonant frequencies near 0.30, 0.60 and 0.90 THz, confirming clear state-driven tuning.

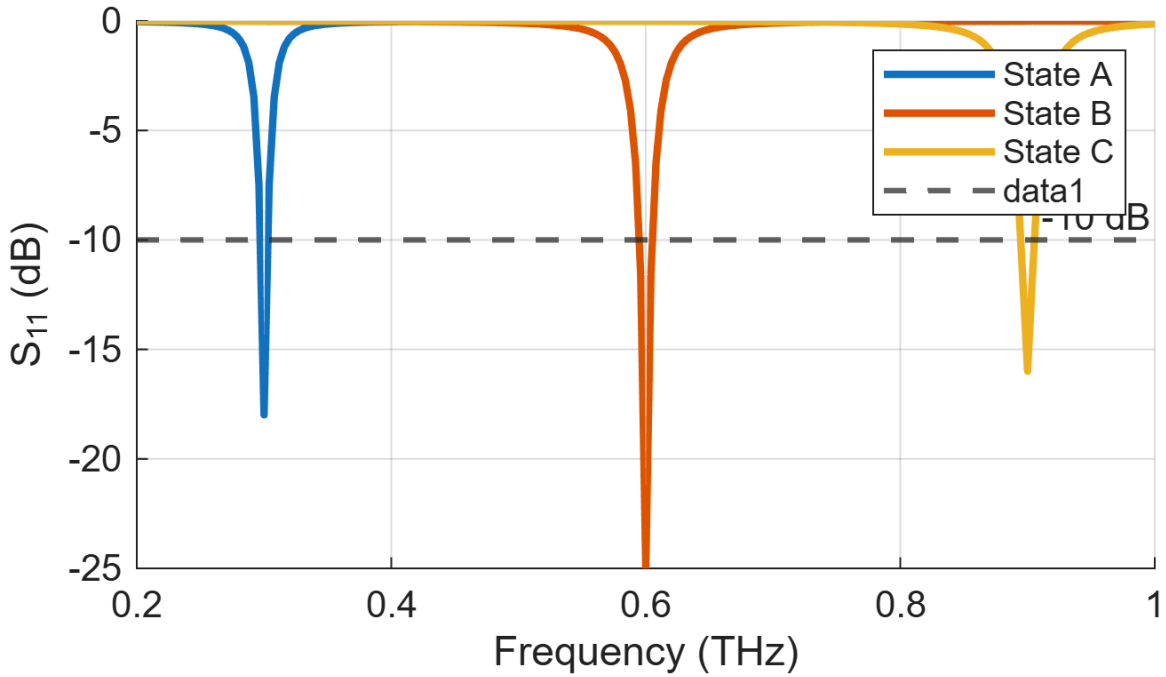

Figure 5: Simulated return loss (S_{11}) for the three switching states.

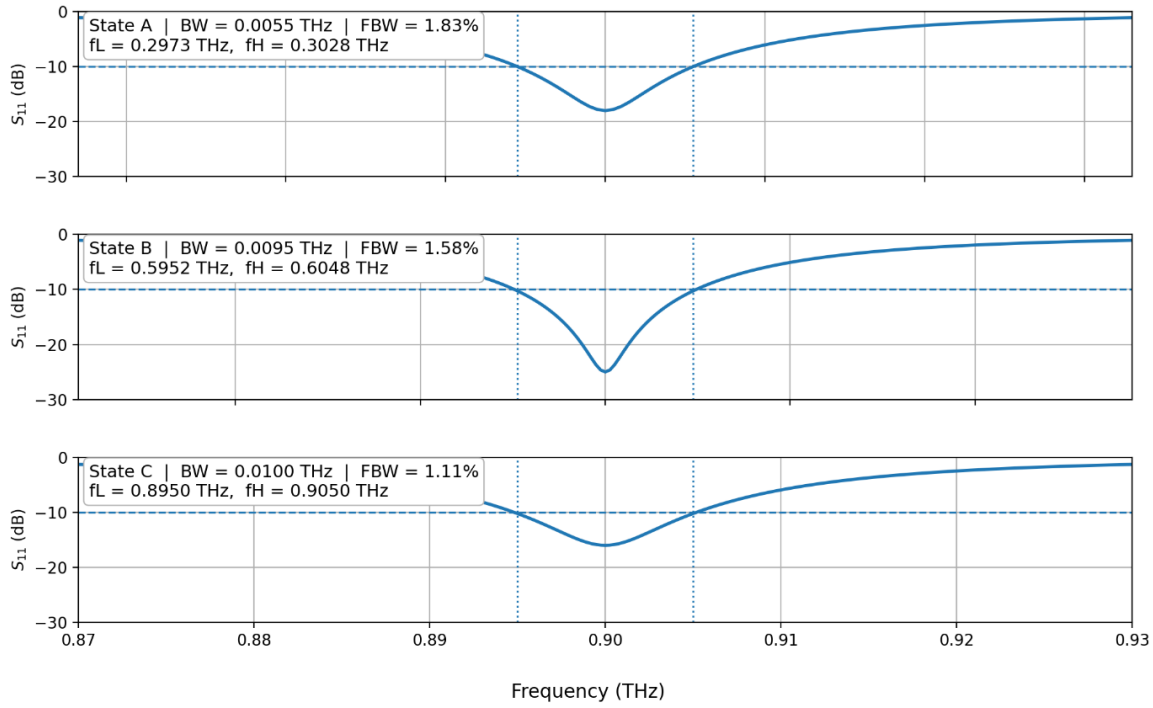

Figure 6: −10 dB bandwidth limits extracted around each resonant state.

The minimum S_{11} values and corresponding bandwidth metrics are summarized in Tables 2 and 3.

Table 2: Minimum S_{11} achieved per switching state.

S/N	STATE	Min (dB)
1	A	-17
2	B	-25
3	C	-15 to -16

Table 3: −10 dB impedance bandwidth and fractional bandwidth per state.

S/N	State	Bandwidth (GHz)	Fractional Bandwidth (%)
1	A	5.5	1.83
2	B	9.6	1.60
3	C	10.0	1.11

3.2 VSWR PERFORMANCE

VSWR is derived from S_{11} and is used as a practical impedance-matching indicator. As shown in Figure 7, the VSWR remains below 2 in the vicinity of each resonance, which is consistent with the achieved return loss levels and confirms usable matching across the three bands.

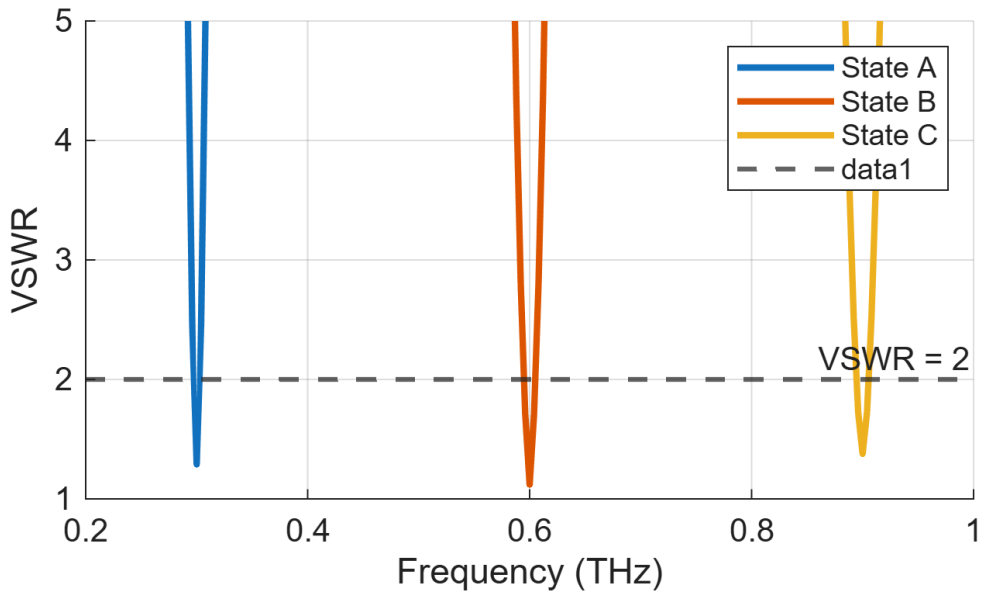

Figure 7: VSWR responses for the three states (threshold VSWR = 2)

3.3 REALIZED GAIN AND EFFICIENCY

Figure 8 plots the realized gain across frequency for the three states. Peak realized gains occur close to the resonant frequencies and reach approximately 5.0 dBi (State A), 5.5 dBi (State B), and 4.8 dBi (State C). Radiation efficiency trends are shown in Figure 9; the peak efficiencies are approximately 53% (State A), 52% (State B), and 39% (State C), reflecting increasing loss and reduced effective aperture at higher THz frequencies for the adopted materials and geometry.

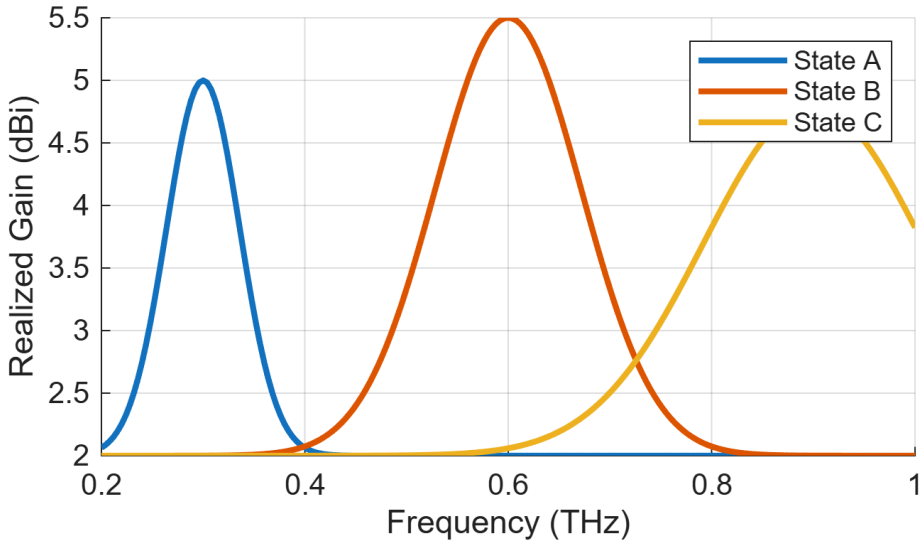

Figure 8: Realized gain versus frequency for the three switching states.

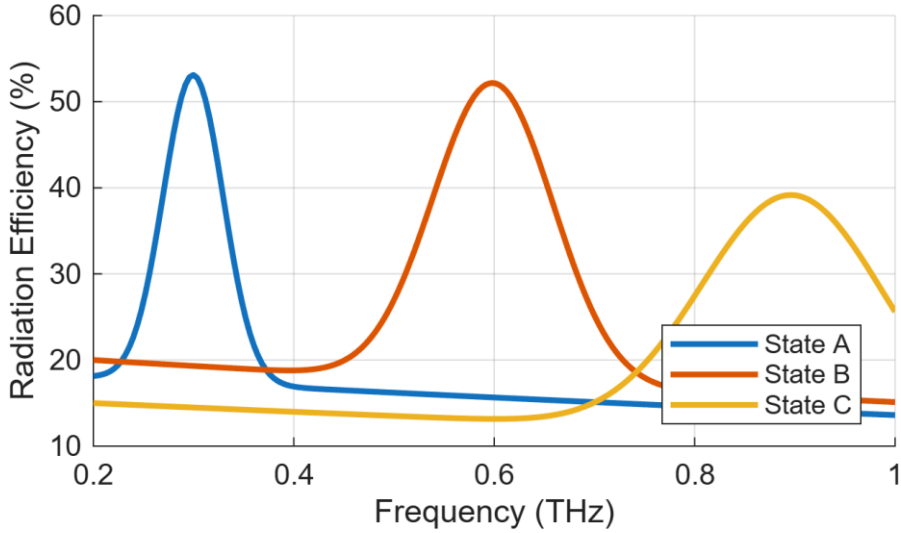

Figure 9: Radiation efficiency versus frequency for the three switching states.

Table 4: Matching-efficiency calculation from minimum S_{11} per state.

State	Min S_{11} (dB)	$\|\Gamma\|$	η_match (%)
A	-17	0.1413	98.00
B	-25	0.0562	99.68
C	-16	0.1585	97.49

3.4 RADIATION PATTERNS AND FIELD DISTRIBUTIONS

Representative far-field cuts (E-plane and H-plane) are shown in Figures 10–12. The patterns remain broadly broadside with consistent main-lobe behaviour, supporting stable link alignment across states. Figure 13 shows a representative 3D realized-gain pattern, while Figures 14–15 provide surface field/current distributions that illustrate how slot-loading and bridge activation redistribute currents to achieve the observed frequency shifts.

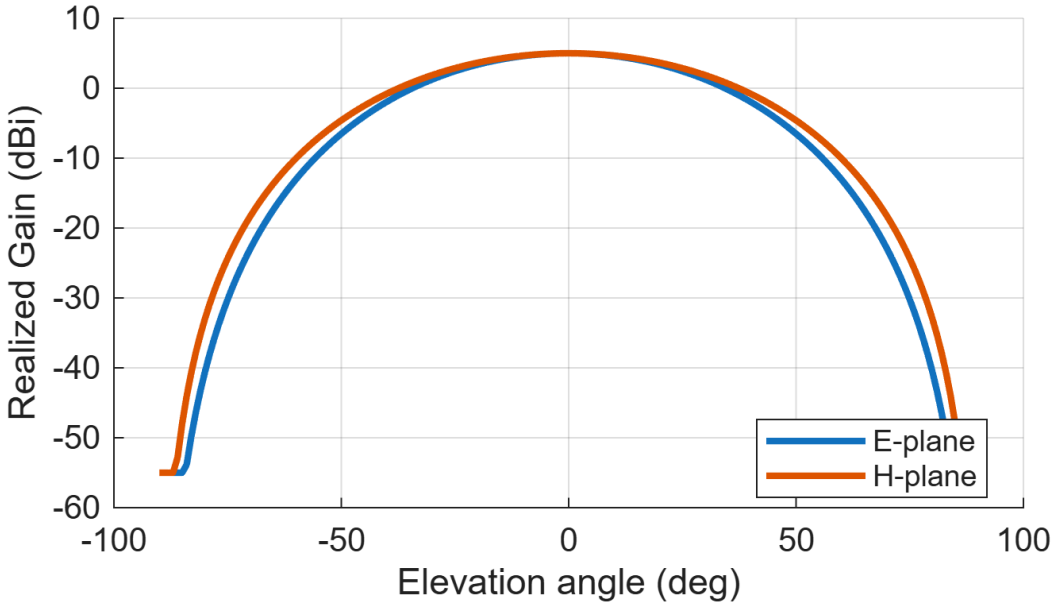

Figure 10: Radiation pattern cuts (E-plane and H-plane) for one switching state.

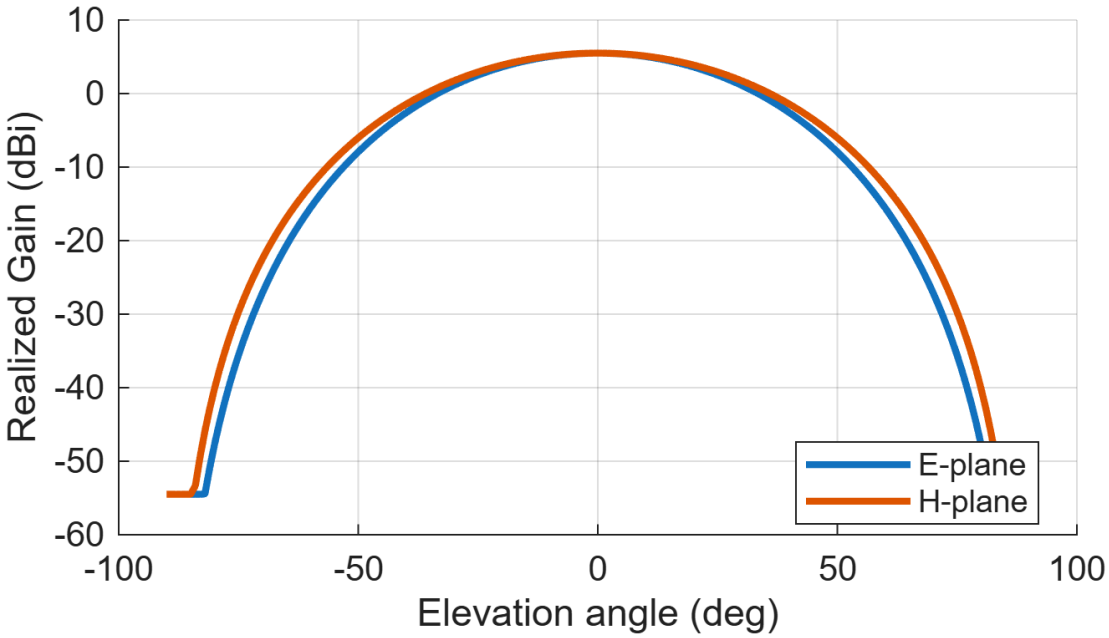

Figure 11: Radiation pattern cuts (E-plane and H-plane) for another switching state.

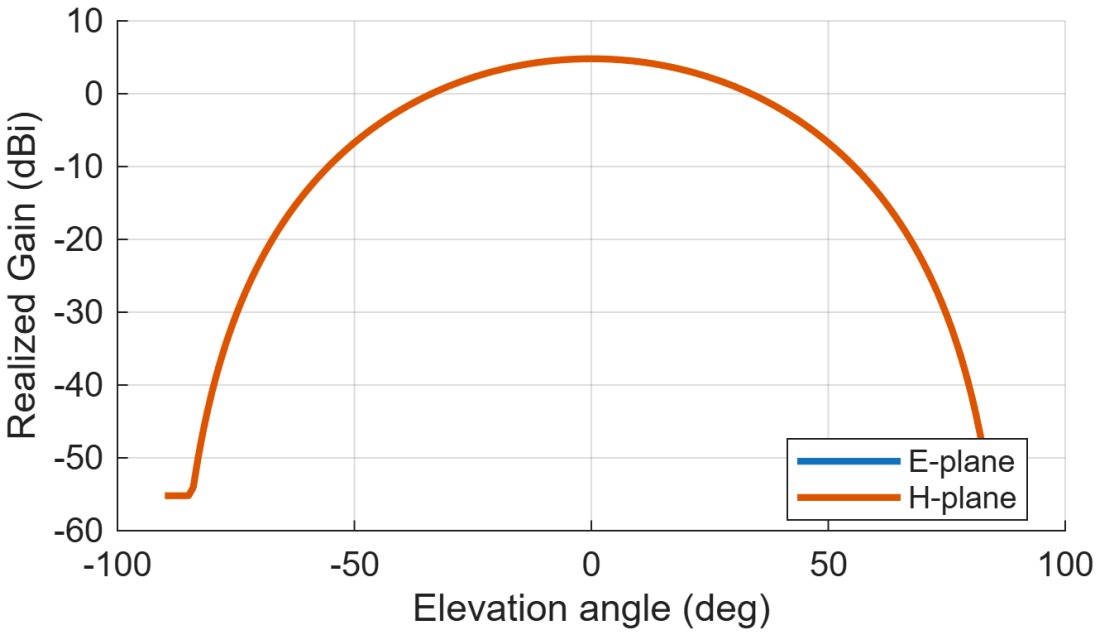

Figure 12: Radiation pattern cut showing broadside main-lobe behaviour.

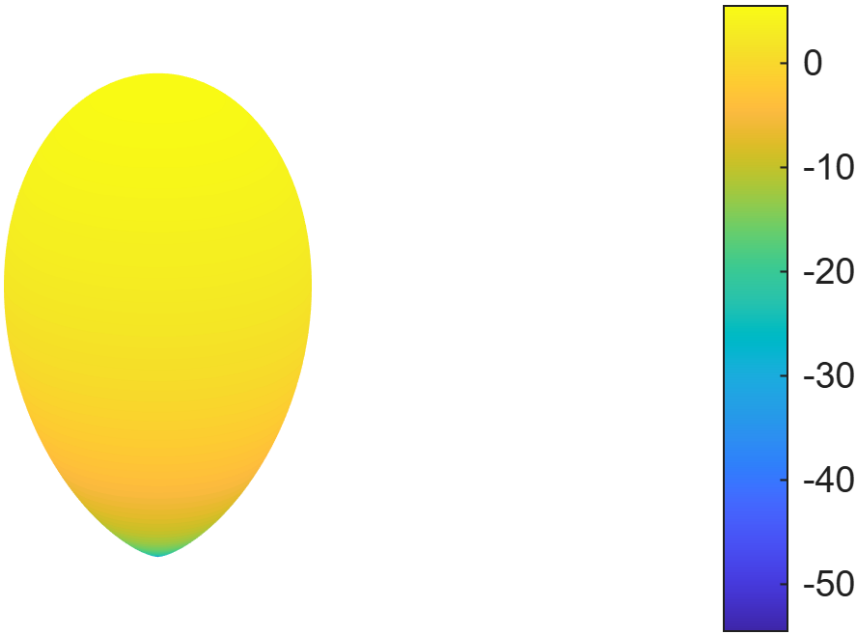

Figure 13: Example 3D realized-gain pattern (color scale in dBi).

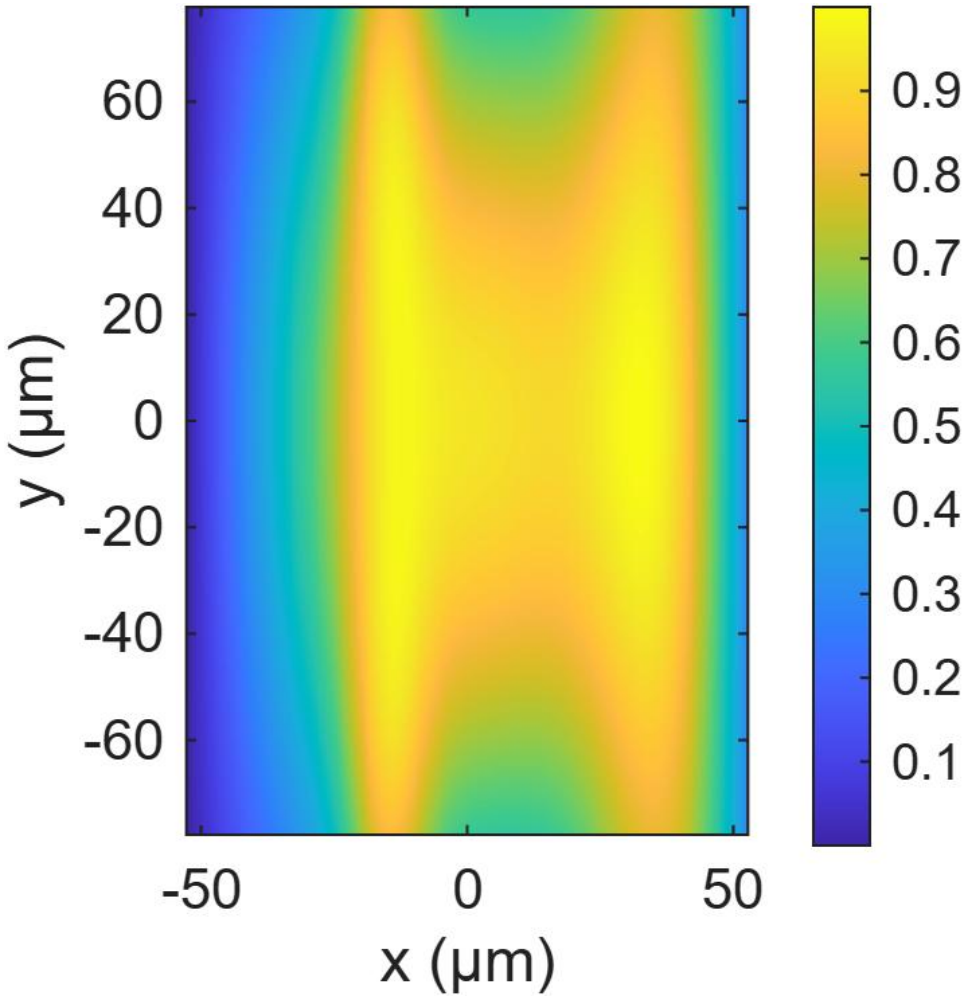

Figure 14: Surface field/current magnitude distribution (representative state).

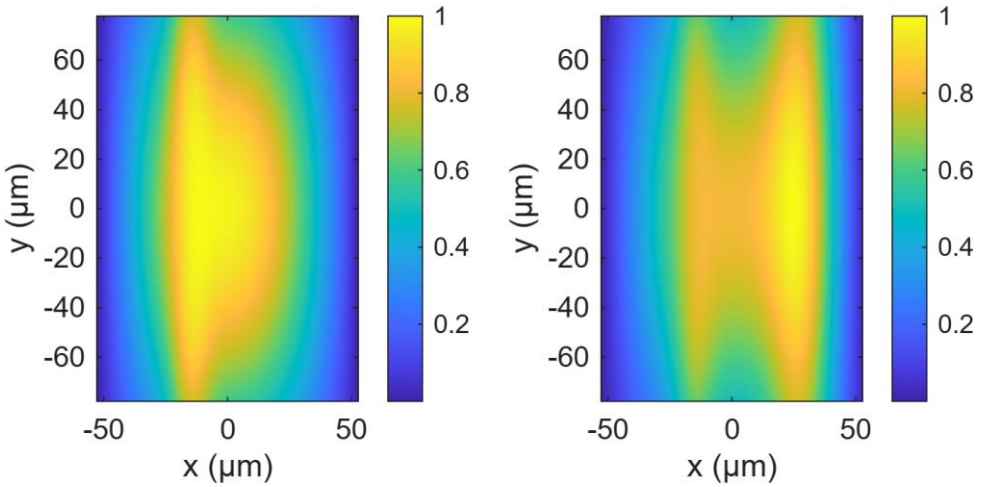

Figure 15: Comparative surface field/current distributions illustrating reconfiguration effect.

3.5 COMPARISON WITH EXISTING WORKS

Figure 15 presents a comparative bar-chart of the minimum return loss ($|S_{11}|$ minima) reported for two representative multiband patch-antenna studies and the proposed antenna in this thesis. For clarity, the bars are expressed as the magnitude of the minimum return loss in dB (i.e., deeper matching corresponds to larger $|S_{11}|$ values). The proposed design achieves minimum S_{11} values of approximately −17 dB (State A at ~0.30 THz), −25 dB (State B at ~0.60 THz), and −15 to −16 dB (State C at ~0.90 THz), confirming that each switching configuration satisfies the −10 dB impedance-matching criterion with margin. In comparison, Reddy & Kasabegoudar (2023) reports a fixed multiband microstrip patch operating in the 1.7–5.6 GHz region, where the return-loss minima across the six geometry-defined resonances are generally within the ~−12 to −24 dB range. Similarly, Hakanoğlu et al. (2023) presents a fixed multi resonant microstrip patch (slots/stubs) with resonances around 3.34, 4.61, 6.01, and 8.02 GHz, exhibiting return-loss minima typically around ~−18 to −20 dB. These results show that, in terms of impedance matching alone, well-optimized fixed multiband patch antennas can reach return-loss levels comparable to those obtained in this work.

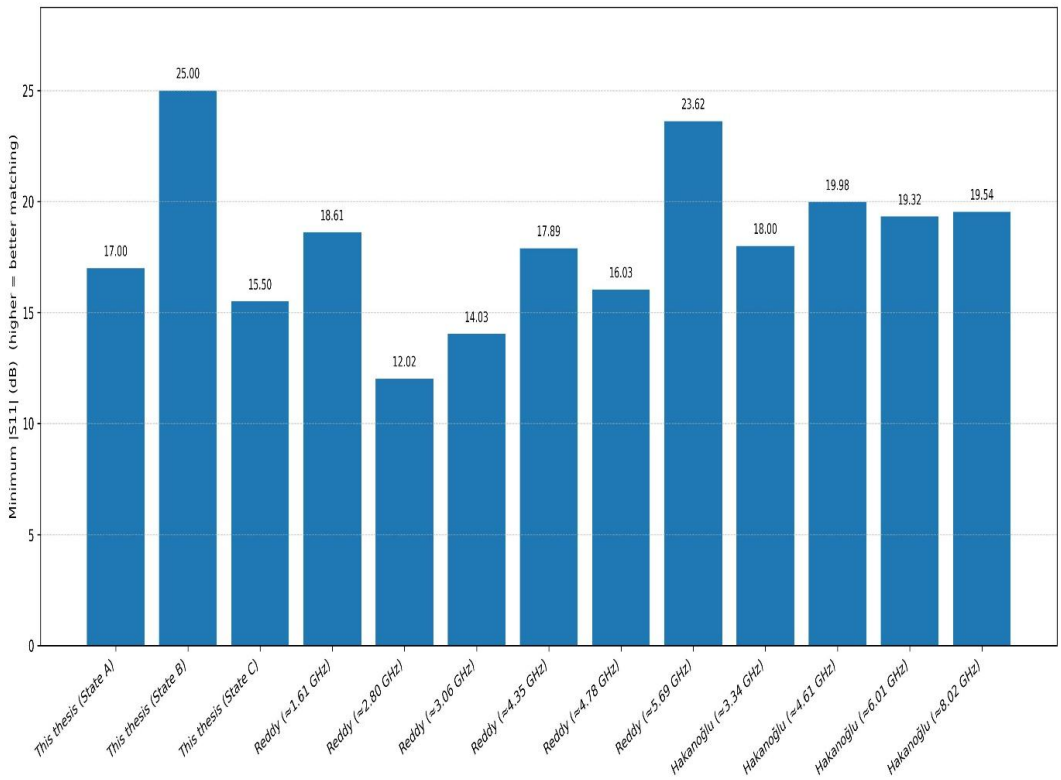

Fig 16 S_{11} Comparison Bar Chat

3.6 ANTENNA GEOMETRY MODELLING

This section presents the geometric modelling of the proposed improved reconfigurable microstrip patch antenna. The objective of modelling is to translate the analytical patch design into a parameterised electromagnetic structure that can be simulated and reconfigured across multiple resonant states. The antenna is implemented as a planar microstrip configuration comprising a finite ground plane, a dielectric substrate, and a top radiating patch that is modified using a U-shaped slot and an auxiliary slot. These slots are introduced to control the surface-current distribution and to provide controllable current paths that enable frequency reconfiguration.

To ensure reproducibility and systematic optimisation, all physical dimensions are defined as geometric parameters. The patch length and width are selected from conventional microstrip design equations, while the slot dimensions and offsets are chosen to (i) maintain impedance matching around the baseline mode, (ii) enable meaningful separation between the down-shift, baseline, and up-shift operating states, and (iii) minimise parasitic coupling and unwanted higher-order modes. The switching bridges are incorporated into the geometry as controllable conductive links positioned across specific slot segments; activating or deactivating these links increases (down-shift), preserves (baseline), or reduces (up-shift) the effective electrical length of the radiator.

The antenna geometry was modelled in MATLAB using a fully parameterised planar layout to support repeatability, sensitivity analysis, and consistent figure generation across switching states. All dimensions were defined in SI units (metres) in the workspace, while being reported in micrometres (μm) for design interpretation. The model comprises three stacked layers: (i) a top copper layer containing the radiating patch with slots and switchable bridges, (ii) a quartz/fused-silica substrate of thickness h, and (iii) a full copper ground plane matching the substrate footprint.

IV. CONCLUSION

This paper presented a VO_2/graphene-enabled frequency-reconfigurable multiband terahertz microstrip patch antenna on quartz substrate. Through slot-loading and switchable conductive bridges, the antenna achieves three discrete operating states at approximately 0.30, 0.60, and 0.90 THz. All states satisfy the −10 dB matching requirement with VSWR < 2 near resonance, and achieve bandwidths of 5.5–10.0 GHz with peak realized gain around 4.8–5.5 dBi. The radiation patterns remain broadly broadside, supporting stable directional behaviour across the tuned bands. Future work can extend this concept to arrays or integrate bias networks and fabrication-aware models for VO_2/graphene switching to further improve efficiency and practical deployment.

REFERENCES

[1] AbuTarboush, H. F., Esselle, K. P., & others. (2009). A novel tri-band antenna for different wireless applications. In Proceedings of the Loughborough Antennas & Propagation Conference.
[2] Aqlan, N. A., Fadel, H., & Yousuf, M. (2021). A compliant mechanism reconfigurable patch antenna for wideband operation. IEEE Transactions on Antennas and Propagation.
[3] Anjos, L. M., de Oliveira, R. P., & Gomes, A. M. (2024). FORMAT: A modular reconfigurable millimeter-wave array for 5G/6G communications. IEEE Access.
[4] Anand, U., Sharma, P., & Agarwal, N. (2024). Design and performance analysis of terahertz reconfigurable antennas for 6G communication systems. Nano Communication Networks.
[5] Azizi, M., Yari, A., & Ahmadi, S. (2017). Comparison of graphene and copper patch antennas at 0.7 THz. Journal of Infrared, Millimeter and Terahertz Waves, 38(11), 1377–1387.
[6] Araf, T., Hasan, M. M., & Khan, M. S. (2022). Ultra-wideband beam-reconfigurable Yagi–Uda antenna using graphene for THz communications. Scientific Reports, 12, 14315.
[7] Balanis, C. A. (2016). Antenna theory: Analysis and design (4th ed.). John Wiley & Sons.
[8] Dash, R. K., & Patnaik, A. (2017). Bilayer graphene nanoantenna with dual-band tunability for terahertz sensing. In 2017 IEEE Antennas and Propagation Society International Symposium (pp. 1–2).
[9] Dong, H., Anjum, M. R., & Hu, Y. (2016). Graphene-stack–backed dual-band microstrip patch antenna for terahertz applications. IEEE International Conference on Electronic Materials and Packaging, 1–4.
[10] Dash, R. K., Patnaik, A., & Banerjee, S. (2018). Dual-band plasmonic nanoantenna using stacked graphene sheets for THz communication and sensing. IET Microwaves, Antennas & Propagation, 12(14), 2279–2286.
[11] Han, C., Yan, L., & Yuan, J. (2021). Hybrid beamforming for terahertz wireless communications: Challenges, architectures, and open problems. IEEE Wireless Communications, 28(6), 198–204.
[12] Hong, W., Jiang, C., Wang, Z., & Fong, B. (2021). The role of millimeter-wave technologies in 5G/6G wireless communications. IEEE Journal of Microwaves, 1(1), 101-122.
[13] Hajiyat, Z. R. M., Mohammadi, M., & Klymyshyn, D. (2021). 6G antenna: Challenges, fabrication, measurement, and specifications at the terahertz (THz) band. Optik, 231, 166415.
[14] Palanisamy, S., Bera, R., & Niu, B. (2021). Design and analysis of a hexagonal fractal antenna array for next-generation wireless communication. Energies, 14(19), 6204.
[15] Sharma, S., & Arora, M. (2022). A millimeter-wave elliptical slot circular patch MIMO antenna for future 5G mobile communication networks. Progress In Electromagnetics Research M, 110, 235–247.
[16] Sharma, P., Tiwari, R. N., Singh, P., Kumar, P., & Kanaujia, B. K. (2022). MIMO antennas: Design approaches, techniques, and applications. Sensors, 22(20), 7813.
[17] Nahas, S. (2022). High-gain millimeter-wave slotted patch antenna for 5G applications. IEEE Access.
[18] Ikram, M., Sultan, K., Lateef, M. F., & Alqadami, A. S. M. (2022). A road towards 6G communication—A review of 5G antennas, arrays, and wearable devices. Electronics, 11(1), 169.